NOTES

A Pulse Sequence for Flow Evaluation Based on Self-Refocused RF and Interleaved Spiral Readout

Atsushi Takahashi,*,† Tie-Qiang Li,‡,§ and Hans Stødkilde-Jørgensen*

*MR Centret, Skejby Hospital Brendstrupgaardsvej, DK-8200 Aarhus N, Denmark; and ‡Karolinska MR Research Center,
Building N8, S-171 76 Stockholm, Sweden

Recently, the use of the phase-contrast method based on interleaved spiral **k**-space acquisition has been demonstrated by Pike *et al.* (*1*) for flow measurements *in vivo.* Gradient-recalled spiral imaging is a fast nuclear-magnetic-resonance imaging technique. The advantages of the spiral-imaging technique rests with the fact that without stringent requirements for the amplitude and slew rate of the gradient system, during only a few free-induction decays, a set of **k**-space data can be collected with sufficient density and extent for reconstructing an image (*2, 3*). Furthermore, it has recently been demonstrated that spiral imaging is less sensitive to distortion and ghosting artifacts from flowing material (*4*), since the first and higher order moments of the spiral readout gradients are zero at the origin of **k** space and increase only slowly and smoothly with **k** space. However, in practice, there are several factors which limit the actual performance of this technique. The first is static field inhomogeneities, causing variation of the point-spread function of the image as a function of offset frequency, leading to geometric distortion affecting the quality of the image. The second factor is the eddy currents produced when switching the gradients. These may be overcome by measuring the actual **k**-space trajectory modified by the eddy currents and compensating for these during the reconstruction procedure (*5*). Another factor is that the large signal bandwidth necessary for fast data acquisition reduces the achievable signal-to-noise ratio. The fourth factor is the off-resonance artifacts from the fat. A long spectral–spatial radiofrequency pulse, typically 15 ms, is usually used to suppress the artifacts from the fat tissues (*6*).

In the applications of spiral imaging to quantitative flow studies of unsteady and turbulent flow, it is very important to keep the slice selection RF and gradient pulses as short as possible in order to eliminate the flow-induced phase artifacts during slice selection. The acquired phase shifts for irregularly moving spins in the presence of long gradient and RF pulses are difficult to calculate and compensate (*7*). In the present study, we present a pulse sequence based on the combination of a self-refocused RF pulse (*8–11*) with spiral readout gradients. This shortens the slice selection by about 12 ms. Furthermore, the self-refocused RF pulse dephases the residual transverse magnetization while it excites the longitudinal component (*12*). With this pulse sequence, we performed velocity-profile measurements for a stenosis model with 75% area reduction in the cross section. The experimental results clearly demonstrate that, using this method, velocity profiles for complex flow can be rapidly and accurately measured with a conventional gradient system.

The pulse sequence is schematically presented in Fig. 1. As shown, the slice selection was achieved by an amplitude-modulated band-selective RF pulse with uniform response and pure phase. The pulse duration is 3.2 ms with a selective bandwidth of 1.25 kHz. The selective RF pulse were designed to focus the transverse magnetization along the real axis in the rotating reference frame. The system hardware has a gradient slew rate and gradient amplitude limits of 17 mT/m/ms and 10 mT/m, respectively. The design of the interleaved spiral readout gradients was based on the variable rate method proposed by Hardy and Cline (*13*). The desired in-plane spatial resolution is 0.84 mm/pixel. Five turns of the spiral trajectory could be achieved with a readout window of 19.2 ms, yielding a field-of-view of 215 mm in 20 interleaves. The first 7.3 ms of the waveforms was limited by the maximum slew-rate constraint, whereas the remainder was limited by the gradient amplitude constraint. The constant-gradient-amplitude portion of the spiral waveforms produces a relatively uniform sampling density function; therefore, some correction was required for only the slew-rate limited portion. At the end of the spiral-readout gradient, trapezoidal spoiler gradients of constant amplitude were applied. Each interleave was realized by rotating the basic
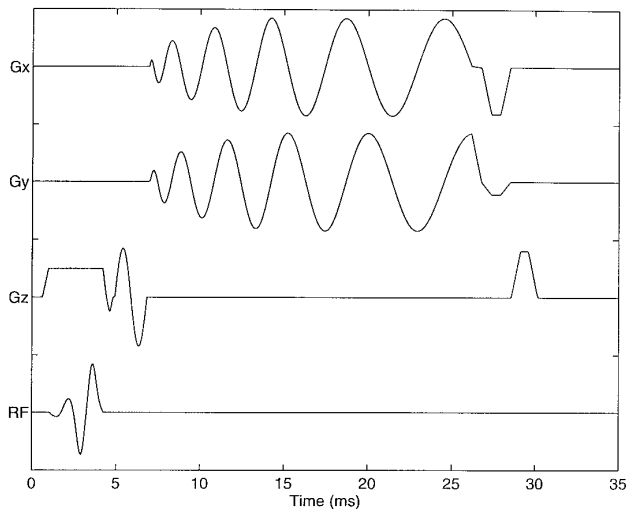
† Current address: Stanford University School of Medicine, Lucas MRS Building, Stanford, California 94305-5488.

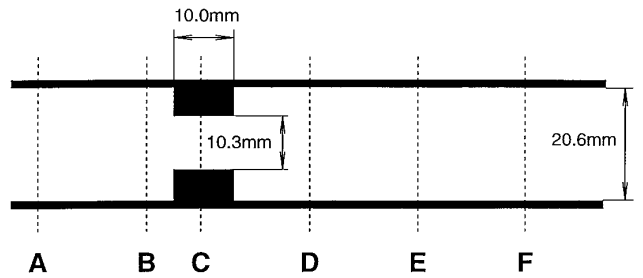§ To whom correspondence should be addressed.

waveforms of the readout gradients around the slice selection axis using the scanner's waveform rotation hardware. The actual **k**-space trajectory was measured with a self-encoding technique (5). The velocity encoding was carried out by using a phase-contrast method with three flow-encoding steps (on, off, and inverse). The amplitude of the velocity-encoding bipolar gradient is chosen to produce a maximum phase shift of π in the images for a given flow rate. The pulse sequence was implemented on a 1.5 T wholebody medical scanner (GE Signa). With a sequence-repetition time of 50 ms, a temporal resolution of one image per second can be achieved.

The image reconstruction was performed off-line on a Sparc-5 Sun workstation using the method outlined by Meyer *et al.* (3). To compensate for the nonuniform *k*-space sampling density, a nonlinear weighting was applied to the raw data, and a gridding procedure was then used to convolve the data sampled in spiral trajectories onto a two-dimensional square matrix. Finally, a 2D fast Fourier transformation (FFT) was performed to produce a 256 × 256 image. The complex image was divided by the Fourier transformation of the gridding kernel to correct the image intensity modulation caused by the convolution.

The flow phantom used is a straight tube (ID = 20.6 mm) with a stenosis giving rise to 75% area reduction in the cross section. The stenosis section is schematically shown in Fig. 2. To improve shimming, the stenosis model was inserted into a larger acrylic cylinder filled with water doped with $MnCl_2$. The length of the straight pipe preceding the stenosis was 2.0 m (L/D 100) to provide sufficient length for the

FIG. 2. A schematic presentation of the stenosis model with 75% area reduction in the cross section. The dashed-lines (A–F) indicate the positions where axial velocity-profile measurements were performed.
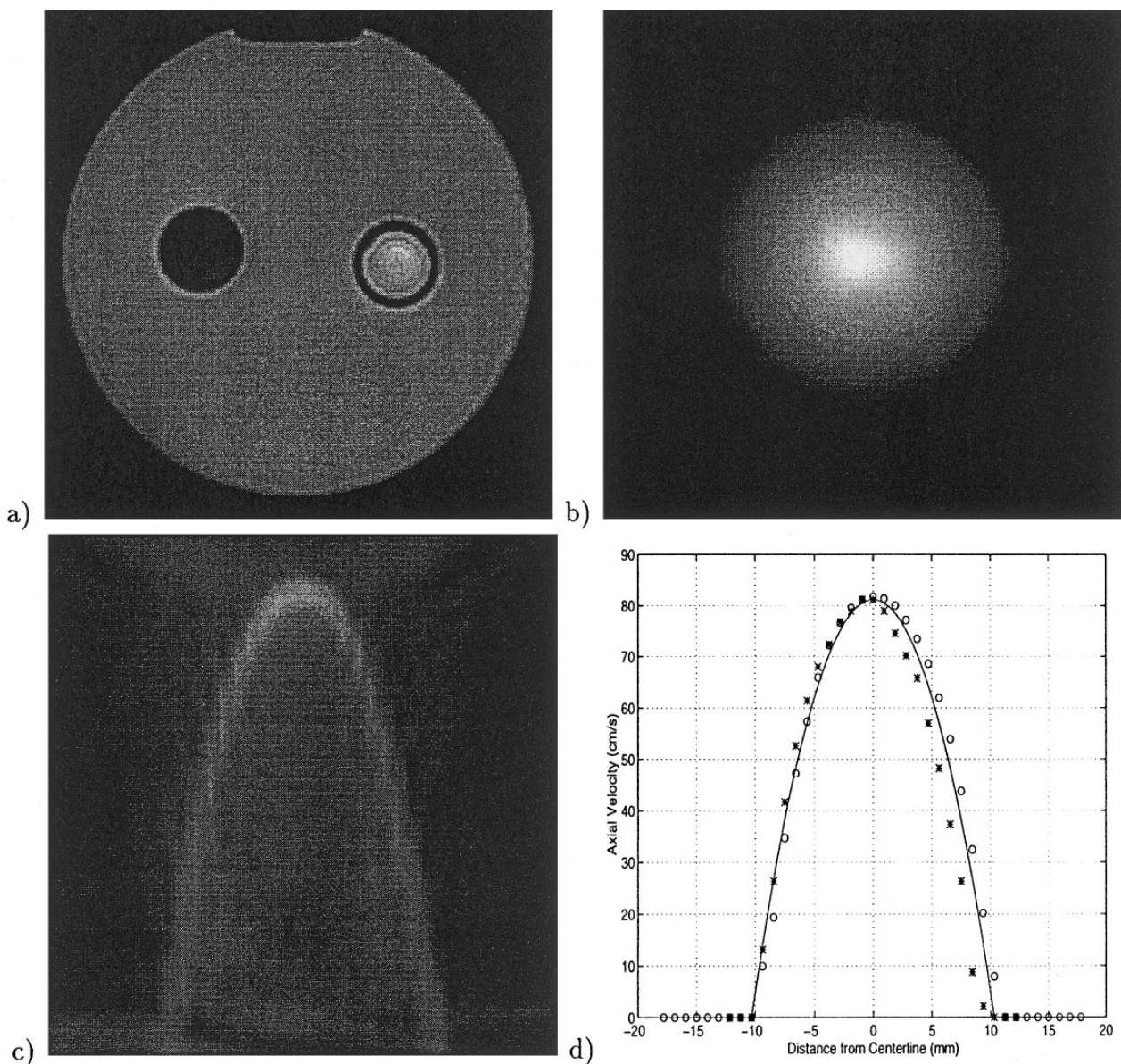
flow profile to develop. To increase the viscosity of the fluid, an aqueous carboxylmethylated cellulose (CMC) solution doped with $MnCl_2$ was used. The viscosity was measured using a falling-ball viscometer. At room temperature, the viscosity of the aqueous CMC solution was 5.6 ± 0.2 centipoise. The flow MRI measurements were performed under the condition of pressure-driven steady flow. The Reynolds number upstream from the contraction was estimated to be Re = 1500. The area-averaged mean bulk flow rate was independently measured by timed collections of the fluid. From the comparison of the bulk flow rate measured in this manner with the NMR imaging results, it was estimated that the NMR data for the axial velocity profile have an error limit of approximately 5%. Flow measurements using phase contrast spiral with spectral-spatial RF, phase contrast based on conventional gradient echo, and Fourier velocity encoding (14, 15) based on a gradient echo which directly visualizes the velocity profiles, were also performed.

Figure 3a shows a modulus image of the phantom acquired in the transverse plane. The stenosis model passed through the circle on the right. The intensity contrast in this circular region was due to the phase flow encoding and the flow in the tube. The axial velocity profiles were measured from the phase difference by performing data acquisitions in which the first moment of the gradient waveform along the flow direction was varied between measurements. This is the so-called phase-contrast velocity encoding. The time-domain NMR signals observed in a flow phase-contrast MRI experiment depend primarily upon fluid density, $\rho(r)$, and velocity, $\mathbf{U}(r)$,

$$s(k) = \int \tilde{\rho}(r)\exp[-2\pi i\mathbf{p}\cdot\mathbf{U}(\mathbf{r})]\exp(-2\pi i\mathbf{r}\cdot\mathbf{k})dr, \quad [1]$$

where

$$\tilde{\rho}(r)$$

$$= \rho(r)\exp\left\{-\frac{t}{T_2} - \gamma^2 D \int_0^t \left[\int_0^{t'} G(t'')dt''\right]^2 dt'\right\} \quad [2]$$

FIG. 1. Spiral-phase-contrast pulse sequence. Slice selection is achieved using a delayed self-refocused pulse and is immediately followed by a bipolar flow-encoding gradient pulse. The flow encoding can be switched on and off or inverted between measurements and can be applied along any direction of interest. The readout gradient waveform produces a spiral trajectory in *k* space.

FIG. 3. The spiral-phase-contrast sequence was calibrated using a well-developed steady laminar flow. (a) The amplitude image in the transverse plane of the phantom. (b) Phase difference acquired with the velocity-encoding gradient on and inverted. (c) Axial velocity profile acquired directly using the Fourier encoding method. (d) The velocity data from spiral-phase-contrast and Fourier velocity-encoding methods are presented by circles and asterisks, respectively. The curve indicates the parabolic flow profile based on the volumetrically measured mean bulk flow rate.

$$2\pi\mathbf{k} = \gamma \int_0^t G(t')\,dt' \quad \text{and} \quad 2\pi\mathbf{p} = \gamma \int_0^t G(t')t\,dt', \quad [3]$$

where $G(t)$ is the time-dependent magnetic field gradient and $\mathbf{r}$ is the spatial position vector. The gyromagnetic ratio, the spin–spin relaxation time, and the self-diffusion constant for ^{1}H in the flow medium are given by γ, T_2, and D, respectively. According to Eq. [1], a Fourier transform of the time-domain NMR signals with respect to the spatial $\mathbf{k}$ space will produce a complex image with phase contrast determined by

$$\Phi = 2\pi\mathbf{p} \cdot \mathbf{U}(\mathbf{r}). \quad [4]$$

As indicated in Eq. [4], the phase difference between the measurements with different p values (the first moment of the velocity-encoding gradient) is proportional to velocity only. Figure 3b shows a phase-difference image at the loca-
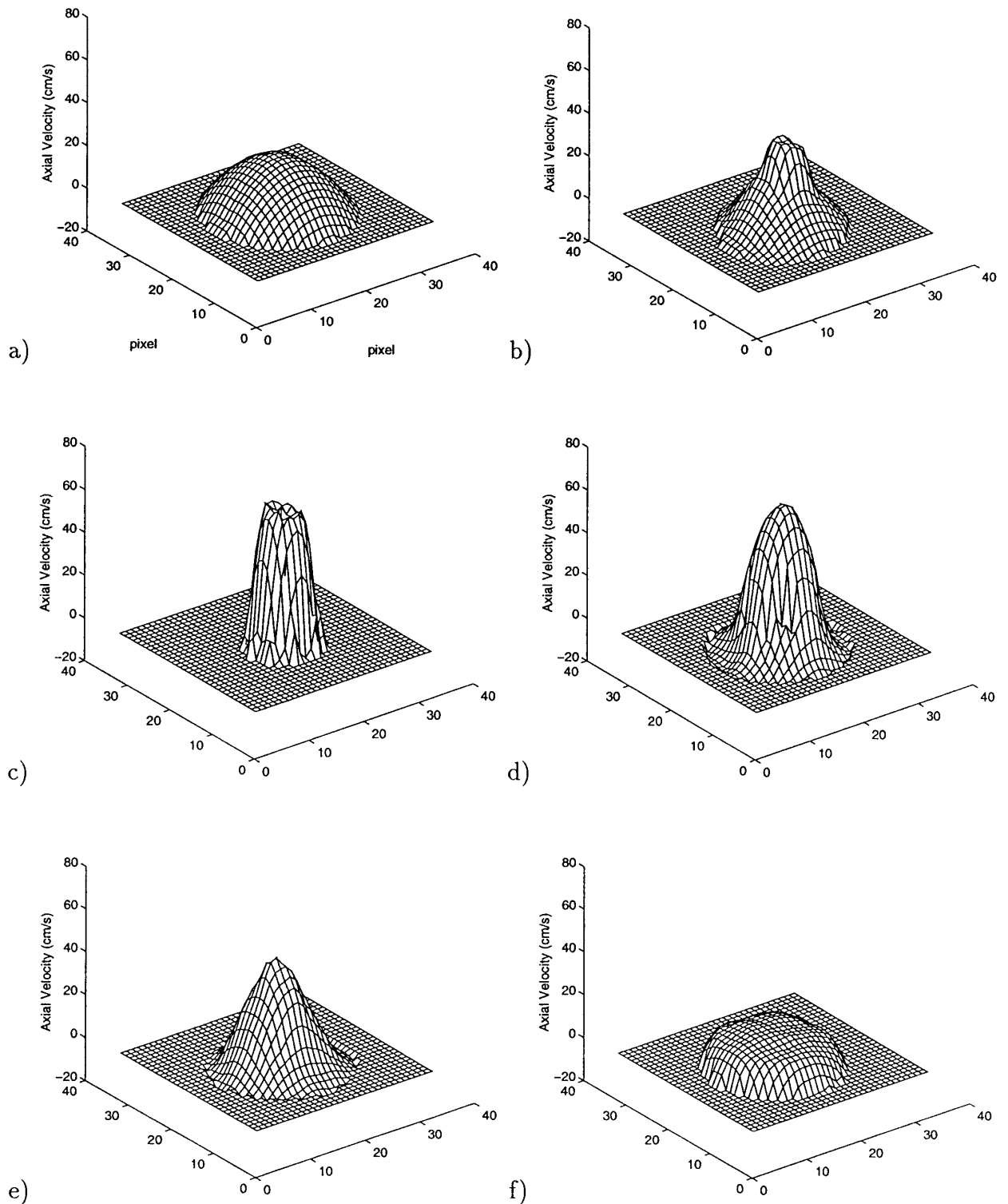
FIG. 4. The axial velocity data acquired using the pulse sequence shown in Fig. 1. The measurements were carried out at different positions both upstream and downstream from the stenosis.

tion far upstream from the stenosis. For an axially symmetric flow system, the axial velocity profile can also be directly visualized by the Fourier velocity-encoding method

(14, 15). In Fig. 3c, the Fourier-encoded velocity-profile upstream from the stenosis is shown. For comparison, the velocity data measured by the phase contrast (Fig. 3b) and

Fourier encoding (Fig. 3c) methods are all presented together in Fig. 3d. The curve is the calculated parabolic velocity profile based on the volumetrically determined mean bulk flow rate. As shown, for well-defined steady laminar flow, the velocity data measured by different methods are consistent with each other within the experimental error limits.

The axial velocity profiles for the stenosis model were measured using the spiral phase-contrast technique with three different types of slice-selection RF pulses, i.e., the self-refocused pulse, spectral-spatial pulse, and sinc pulse. The phase contrast measurements based on conventional gradient echo and Fourier flow-encoding were also performed at different locations both upstream and downstream from the stenosis. With a single repeated signal acquisition, the signal-to-noise ratios of the data acquired downstream using a conventional (spin warp) gradient-echo phase contrast and Fourier-encoding method were too low to permit any quantitative analysis. The data acquired downstream from the stenosis, using the phase-contrast spiral with a spectral-spatial RF pulse or sinc RF pulse, also exhibit severe artifacts resulting from the flow instability. This is somewhat expected, since the flow artifacts due to higher-order velocity fluctuations are drastically more dependent upon the duration of the gradient pulse, as demonstrated by analyzing the fluctuation-induced phase shift using a Taylor series expansion to describe the time-dependent spin positions (16). For MRI studies of turbulent flow, short echo time is, therefore, an essential parameter that determines the signal-to-noise ratio of the images. For example, the FID-acquired-echo (FAcE) sequence minimizes the echo time using fraction-echo acquisition (17). With the FAcE technique, turbulent pipe flow with Reynolds number up to 10,000 can be recorded with reasonably good quality. However, the total data-acquisition time for FAcE is unacceptably long. The phase-contrast method based on spiral readout has a short echo time and a short total data-acquisition time. Combined with a self-refocused RF pulse, the echo time is further reduced by eliminating the rephasing slice-selection gradient lob and by moving the effective excitation time to the end of the RF pulse. Although the spectral-spatial RF pulse is also prefocused, it is apparently not optimized for the reduction of flow artifacts due to the long duration as well as the complicated pulse shape of the slice-selection gradient. Compared to a sinc RF pulse with the same selective bandwidth, using the self-refocused RF pulse can reduce the echo time by approximately 2 ms, which is quite a significant improvement for turbulent-flow studies. It should be pointed out that using a small-flip-angle sinc RF pulse does not necessarily reduce the amplitude and duration of the slice-selection gradient, which are determined by the slice thickness and the RF bandwidth. The possibility of reducing flow artifacts using self-refocused RF has been demonstrated previously by Gate *et al.* (7) using a conventional gradient-recalled-echo pulse sequence. As demonstrated in the present study,
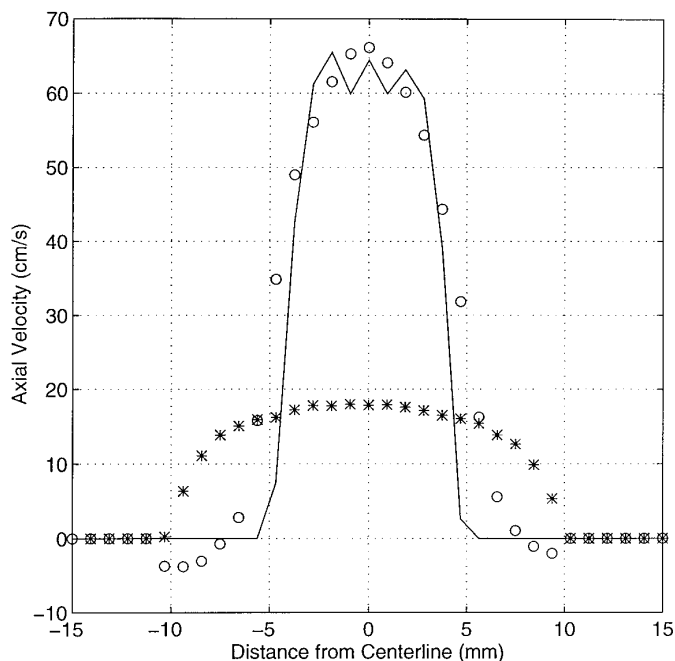

FIG. 5. Development of the post-stenotic velocity profiles across the symmetric axis. The symbols, —, ○, and * represent axial velocity profiles at the axial positions (as shown in Fig. 2) c, d, and f, respectively.

the signal-to-noise ratios of the phase contrast data for turbulent flow can be improved significantly by combining the self-refocused RF pulse with interleaved spiral readout.

Figure 4 shows the axial velocity profiles at six different positions measured using the spiral pulse sequence shown in Fig. 1. The corresponding slice positions are indicated by dashed lines (A–F) in Fig. 2. Far upstream from the stenosis, we observed a nearly perfect parabolic velocity profile (Fig. 4a). Ahead of the stenosis, the fluids in the centerline regions accelerate (Fig. 4b). A quite blunted flow profile was observed in the residual lumen area. The flow in the stenotic section became turbulent, since the Reynolds number was doubled due to the diameter reduction of the stenotic segment (Re = 3000). The irregularity of the velocity profiles in this region (Fig. 4c) is most probably due to the turbulent velocity fluctuations. Immediately downstream from the stenosis, we saw the flow separation caused by the poststenotic dilatation (Figs. 4d and 4e). The separation zone appears because of the retrograde hydrodynamic pressure gradient exceeds the fluid momentum in the forward direction. The high velocity and low pressure in the stenotic lumen changes to lower velocity and higher pressure as the cross section expands. In the centerline region where the forward momentum is high, no reversal of flow is observed, whereas near the tube wall where the velocity and the forward fluid momentum is low, the retrograde pressure gradient results in the change in flow direction. Flow instability was also observed in this region and this behavior is typical for a con-

fined jet. As the flow propagates further downstream, the steady laminar flow profile slowly recovers (Fig. 4f). The development of the post-stenotic velocity profiles with downstream distance is collected in Fig. 5. As shown, the deviation from the prestenotic steady laminar flow is very significant. It has been reported that these deviations from prestenotic flow field are significant even in mild obstructions and subcritical stenosis which do not result in severe energy loss and flow reduction (*18*). Rapid and accurate detection of the poststenotic velocity disturbances is useful to diagnose early subclinical occlusive arterial disease.

The main advantages of the interleaved spiral-phase-contrast pulse sequence with the self-refocused RF pulse are the short slice-selection duration, short echo time, short overall data-acquisition time, and the applicability in a conventional imaging system. This makes it possible to produce rapid and accurate velocity measurements for complex and unsteady flows. Experimental results from a well-defined stenosis model demonstrated a significant improvement in signal-to-noise ratio of the acquired flow images. This pulse sequence can be directly used for complex flow studies of engineering problems, such as opaque and multiphase systems (*19*) where conventional flow measurement techniques are inaccessible. For *in vivo* applications where chemical-shift artifacts due to fat tissues could be problematic, other lipid-suppression schemes must be employed.

ACKNOWLEDGMENTS

REFERENCES

1. G. B. Pike, C. H. Meyer, T. J. Brosnan, and N. J. Pelc, *Magn. Reson. Med.* **32**, 476 (1994).

2. C. B. Ahn, J. H. Kim, and Z. H. Cho, *IEEE Trans. Med. Imaging.* **MI-5**, 2 (1986).

3. C. H. Meyer, B. S. Hu, D. G. Nishimura, and A. Macovski, *Magn. Reson. Med.* **28**, 202 (1992).

4. D. G. Nishimura, P. Irarrazabal, and G. H. Meyer, *Magn. Reson. Med.* **33**, 549 (1995).

5. A. Takahashi and T. Peters, *Magn. Reson. Med.* **34**, 446 (1995).

6. C. H. Meyer, J. M. Pauly, A. Macovski, and D. G. Nishimura, *Magn. Reson. Med.* **15**, 287 (1990).

7. A. R. C. Gates, T. P. L. Roberts, N. J. Shah, T. A. Carpenter, and L. D. Hall, *J. Magn. Reson.* **96**, 222 (1992).

8. H. Geen, S. Wimperis, and R. Freeman, *J. Magn. Reson.* **85**, 620 (1989).

9. X. L. Wu, P. Xu, and R. Freeman, *Magn. Reson. Med.* **20**, 165 (1991).

10. H. Geen and R. Freeman, *J. Magn. Reson.* **93**, 93 (1991).

11. G. C. McKinnon, *Magn. Reson. Med.* **29**, 260 (1993).

12. T. P. L. Roberts, T. A. Carpenter, and L. D. Hall, *J. Magn. Reson.* **91**, 204 (1991).

13. C. J. Hardy and H. E. Cline, *J. Appl. Phys.* **66**, 1513 (1989).

14. A. Caprihan and E. Fukushima, *Phys. Rep.* **198**, 195 (1990).

15. T. Q. Li, J. D. Seymour, R. L. Powell, K. L. McCarthy, L. Ödberg, and M. J. McCarthy, *Magn. Reson. Imaging* **12**, 923 (1994).

16. Q. S. Xiang and O. Nalcioglu, *IEEE Trans. Med. Imaging* **MI-6**, 14 (1987).

17. M. B. Scheidegger, S. E. Maier, and P. Boesiger, *Magn. Reson. Imaging* **9**, 517 (1991).

18. X. P. Lefebvre, E. M. Pedersen, J. Ö. Hjortdal, and A. P. Yoganathan, *in* ''Vascular Imaging by Color Doppler and Magnetic Resonance'' (P. Lanzer and A. P. Yoganathan, Eds.), p. 51, Springer-Verlag, Berlin/New York, 1991.

19. T. Q. Li, J. D. Seymour, R. L. Powell, K. L. McCarthy, M. J. McCarthy, and L. Ödberg, *AIChE J.* **40**, 1408 (1994).